Doping-dependent character and possible magnetic ordering of NdNiO$_2$

Frank Lechermann

European XFEL, Holzkoppel 4, 22869 Schenefeld, Germany
and Center for Computational Quantum Physics,
The Flatiron Institute, 162 5th Avenue, New York, New York 10010, USA

The novel nickelate superconductors of infinite-layer type feature challenging electronic pecularities in the normal-state phase diagram with doping. Distinct many-body behavior and different dispersion regimes of the entangled {Ni-d_{z^2}, Ni-$d_{x^2-y^2}$} orbital sector give rise to highly rich physics, which is here studied for the case of the NdNiO$_2$ system. An analysis based on advanced realistic dynamical mean-field theory unveils that the superconducting hole-doped region is the meeting place of a (self-)doped Mott insulator from the underdoped side, and a bad Hund metal from the overdoped side. Fermi-level crossing of the Ni-d_{z^2} flat-band ties both regimes together to form a singular arena for unconventional superconductivity. We furthermore shed light on the intriguing problem of elusive magnetism in infinite-layer nickelates. Antiferromagnetic (AFM) order with small Ni moments is shown to be a vital competitor at low temperature. At stoichiometry, C-AFM order with ferromagnetic spin-alignment along the c-axis benefits from a conceivable coexistence with Kondo(-lattice) screening.

I. INTRODUCTION

Nickelate superconductivity in thin films of Sr-doped NdNiO$_2$ below a critical temperature $T_c \sim 10$ K entered the scene in summer 2019 [1]. Recently, the same physics has also been identified in Sr-doped PrNiO$_2$ films [2,3]. Because of the sophisticated sample preparation and the so far lack of bulk single crystals, experimental progress on these Ni($3d^9$)-based infinite-layer systems is challenging.

Several findings still enable further insight into a very rich phyenomenology. Ordered magnetism is hard to measure in the thin-film geometry, but neutron scattering on polycrystalline bulk samples provides no clear evidence for long-range antiferromagnetic (AFM) order in NdNiO$_2$ [4,5]. However, recent nuclear-magnetic-resonance (NMR) experiments [6] on similar samples suggest quasistatic AFM ordering for $T < 40$ K. This, together with a resistivity upturn [1] below $T \sim 70$ K, points to intriguing low-energy physics even far from the superconducting region. That region is sandwiched between weakly insulating doping regimes in the range $0.125 \lesssim x \lesssim 0.25$ of the phase diagram for hole doping x of Sr kind [7,8]. Doping-dependent Hall data [7,8] point to a two-band scenario with x. First spectroscopic results reveal hybridization of Ni($3d$) states with other delocalized states and reduced Ni-O intermixing compared to NiO and LaNiO$_3$ [9]. Furthermore, for finite x, a substantial Ni($3d^8$) character is unveiled [10,11], in contrast to the dominant Cu($3d^9\underline{L}$), i.e., Cu($3d^9$) with ligand hole on oxygen, weight in high-T_c cuprates. This Ni($3d^8$) signature is either attributed to multiorbital physics [10] or to Ni($S=0$) single-orbital physics of the $d_{x^2-y^2}$ kind [11]. Concerning the superconducting state, a small anisotropy in the upper critical field, hinting toward a Pauli-limited coupling, as well as a two-symmetry gap nature are reported [12–14].

From the theoretical side, assessments based on density functional theory (DFT) highlight the self-doping (SD) nature of an otherwise seemingly cuprate-like band structure [15–19]. The weakly filled SD band originates from Nd($5d$)-Ni($3d$) hybridization and causes a multisheeted Fermi surface at stoichiometry. There seems also agreement that the charge-transfer character of NdNiO$_2$ is reduced compared to estimates in akin cuprates [18,20]. Further beyond DFT, two main theory concepts are pursued: either (decorated) single-Ni-orbital physics of Ni-$d_{x^2-y^2}$ type [15–17,21–27] or multiorbital Ni($3d$) processes [18,19,28–36] are assumed key to the correlation phenomenology. In two previous works [18,19], we showed that, based on calculations utilizing the combination of DFT with dynamical mean-field theory (DMFT) and furthermore including explicit Coulomb interactions on oxygen, the relevance of Ni-multiorbital degrees of freedom is indeed inevitable. In addition to the indisputable Ni-$d_{x^2-y^2}$ orbital and its related low-energy band, the Ni-d_{z^2} orbital plays a further crucial role. First, in mediating a Kondo(-lattice) coupling between Ni($3d$) and Nd($5d$) at stoichiometry. And second, for establishing a unique flat-band scenario in the doping region of low-T superconductivity.

In the present work, the goal is to extend our previous studies and shed further light onto the Ni-multiorbital physics in infinite-layer nickelates. In Refs. [18,19], paramagnetism was assumed and doping was addressed by a supercell description [18] as well as within a minimal three-band model solved for a simplified Fermi-liquid setting [19]. Here, we provide a detailed account of the doping-dependent features of the correlated electronic structure based on the virtual-crystal approximation, and additionally investigate the intriguing problem of magnetic ordering in the NdNiO$_2$ system.
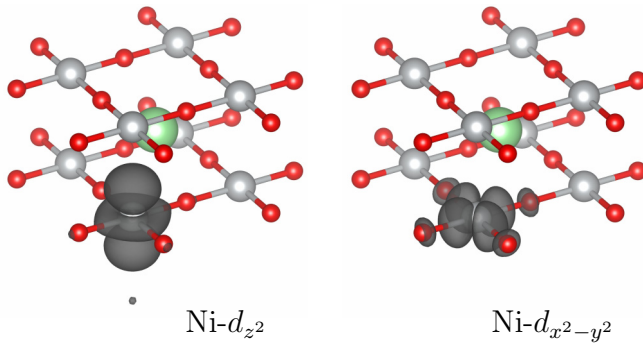
FIG. 1. Projected local orbitals of Ni-d_{z^2} (left) and Ni-$d_{x^2-y^2}$ (right) type in the NdNiO$_2$ compound: Ni(grey), Nd(large,green), O(small,red).

II. METHODOLOGY

The NdNiO$_2$ compound crystallizes with $P4/mmm$ space group, giving rise to a four-atom unit cell (see Fig. 1 for the enlarged cell). The occupied Wyckoff positions amount to 1a:(0,0,0) for Ni, 1d:(0.5,0.5,0.5) for Nd as well as 2f:(0.5,0,0) for O. Stoichiometric lattice parameters are taken from the experiment [1], reading $a = 3.92$ Å and $c = 3.31$ Å.

A. DFT + sicDMFT framework

The charge self-consistent combination [37,38] of DFT and DMFT with the additional incorporation of the self-interaction correction (SIC) is used to investigate the normal-state properties of pristine and doped neodynium nickelate in the infinite-layer structure. The realistic part of this DFT + sicDMFT scheme [39] builds up on a mixed-basis pseudopotential representation [40–42] in the local density approximation (LDA). Coulomb interactions on oxygen are addressed beyond DFT within SIC applied to the O pseudopotential. On the transition-metal (TM) sites, those interactions are treated within DMFT. All three contributions, i.e., DFT, SIC, and DMFT are coupled within a fully charged self-consistent framework that is iterated until convergence of the correlated electronic structure is reached.

A detailed account of the utilized SIC construction can be found in Ref. [43] and references therein. Let us here recapitulate only the main equations on the (pseudo)atomic level, i.e.,

$$(-\nabla^2 + V_l + V_{\mathrm{H}}[n_v] + V_{\mathrm{xc}}[n_v] + V_{\mathrm{cor}}[n_l])\Psi_l^{pp} = \epsilon_l^{pp}\Psi_l^{pp} , \tag{1}$$

$$V_{\mathrm{cor}}[n_l] = -w_l[V_{\mathrm{H}}[n_l] + V_{\mathrm{xc}}[n_l]] , \tag{2}$$

$$V_l^{\mathrm{SIC}}(r) := V_l(r) - \alpha\langle\Psi_l^{pp}, V_{\mathrm{cor}}[n_l]\Psi_l^{pp}\rangle\Psi_l^{pp}(r) , \tag{3}$$

where $\langle\cdots,\cdots\rangle$ marks the scalar product. In Eq. (1) the standard norm-conserving pseudopotential V_l for angular-momentum quantum number l, Hartree potential V_{H}, and exchange-correlation potential V_{xc} for the density n_v of all valence electrons, as well as the correction potential V_{cor} govern the wave function Ψ_l^{pp}. Thereby, $n_v = \sum_l n_l$ with $n_l = p_l|\Psi_l^{pp}|^2$ as the density of electron orbital l. The potential V_{cor} given in Eq. (2) aims at canceling the apparent

self interaction within orbital l [44]. The weight factors w_l between 0 and 1 take care of adjusting the SIC correction to the crystal environment in view of the orbital occupations. Here, while the O(2s) orbital is by default fully corrected with $w_{2s} = 1.0$, the reasonable choice [39,43] $w_{2p} = 0.8$ is used for the O(2p) orbitals. The resulting SIC PP in Eq. (3) is of Kleinman-Bylander operator form and includes an additional parameter α. That second parameter proves useful to take are of further screening properties from the crystal environment. As in previous DFT + sicDMFT works [18,19,39] we used $\alpha = 0.8$, i.e., $\alpha = w_{2p}$ holds as a single SIC parameter.

Introducing SIC for oxygen hence invokes a recomputation, and effective localization [45], of the O orbitals, resulting in a revised r-dependent pseudopotential. Focussing on O(2p), this leads to two key effects: the onsite level energy is modified, attributed to an effective U_{pp}, and the binding properties to Ni(3d) altered, attributed to an effective U_{pd}. As a result, the pd-splitting is enlarged and O(2p)-hybridized dispersions are narrowed. Albeit still on an effective single-particle level, these corrections thus carry over some energy dependence, while the standard DFT + U scheme [46] via its Hartree-Fock structure promotes essentially a high-energy correction. Moreover, note that explicit symmetry breakings are not necessary to obtain the SIC effects.

The inclusion of explicit oxygen-based correlations beyond conventional DFT + DMFT for the NdNiO$_2$ system is believed necessary for mainly two reasons. First, generally, in nickelates as late TM oxides the charge-transfer aspect is stronger as in early TM oxides, and therefore Coulomb interactions from O(2p) will have a larger impact [47–49]. Second, while Ni-$d_{x^2-y^2}$ is strongly hybridized with O(2p) in the infinite-layer structure, Ni-d_{z^2} is less so since there is no apical oxygen (see Fig. 1). Thus especially the Ni-e_g $\{z^2, x^2 - y^2\}$ orbitals of the DMFT-active Ni(3d) shell are quite differently affected by O(2p) and therefore it should be insufficient to treat the Coulomb interactions from oxygen only implicitly via a chemical-potential or Coulomb-on-Ni shift. In Appendix A, we provide a brief comparison between the DFT + sicDMFT and DFT + DMFT picture of pristine and doped NdNiO$_2$.

B. Calculational settings

A $13 \times 13 \times 13$ k-point mesh is utilized for the basic NdNiO$_2$ unit cell. This mesh is reduced for the magnetically ordered supercells as to display the same k-point density for enabling total-energy comparisons. The plane-wave cutoff energy is set to $E_{\mathrm{cut}} = 16$ Ry and local basis orbitals are introduced for Nd(5d), Ni(3d), as well as O(2s, 2p). The Nd(4f) states are put in the pseudopotential frozen core since they are not decisive for the key physics of infinite-layer nickelates [21]. This also means that f-electron-based magnetism is not considered in this work. As in many other comparable compounds, due to the local nature of the $4f$ moments and their weak exchange coupling, magnetic ordering of Nd moments is believed to occur at very low temperatures. Note, furthermore, that the j-resolved frozen occupation of the Nd(4f) shell is here chosen with small resulting moment. The role of spin-orbit effects in the overall crystal calculations is neglected. Additional details for the computation of the

magnetically ordered phases in this work will be given in Sec. IV.

To facilitate the description at finite doping, we here employ the virtual-crystal approximation (VCA) in the fully charged self-consistent scheme. This amounts to replacing the Nd atom by a pseudoatom of nuclear (and electronic) charge $\mathcal{Z} = Z_{\mathrm{Nd}} - \delta$ in the pristine unit cell. As a choice, the charge content of the Nd($4f$) shell is here not modified by this construction. It is then assumed that $\delta = x$ holds, i.e., the VCA doping δ mimics the true Sr doping x of effectively replacing Nd^{3+} by Sr^{2+}. As with any theoretical doping description, the VCA also misses certain effects, e.g., local-structural distortions or correct local charge states of the impurity. But it usually provides a faithful description of the overall effects of charge doping. Note that in the previous works Refs. [18,19], the other two standard options to describe doping, namely supercell [18] and chemical-potential shift [18] have been put into practice. Thus the present perspective completes the conventional method spectrum in that regard.

The DMFT-correlated subspace is governed by a full Slater Hamiltonian applied to the Ni($3d$) projected-local orbitals [50]. The projection is performed on the $6 + 5 + 1 = 12$ Kohn-Sham (KS) states above the dominant O($2s$) bands, associated with O($2p$), Ni($3d$), and the self-doping band. A Hubbard $U = 10$ eV and a Hund exchange $J_{\mathrm{H}} = 1$ eV prove reasonable for this choice of the energy window in the given nickelate [18,19,39]. The fully localized-limit double-counting scheme [51] is applied. Continuous-time quantum Monte Carlo in hybridzation expansion [52] as implemented in the TRIQS code [53,54] is utilized to handle the DMFT problem. The system temperature is set to $T = 30$ K to properly approach the competition/cooperation between quasiparticle (QP) formation, Mott criticality, Kondo physics, and magnetic order in these challenging nickelates. Up to 2×10^9 Monte Carlo sweeps are performed for the respective final convergence steps. A Matsubara mesh of 2049 frequencies is used to properly account for the low-temperature regime. The standard maximum-entropy [55] and Padé [56] method are employed for the analytical continuation from Matsubara space onto the real-frequency axis. If not otherwise stated, all shown data are obtained within charge self-consistent DFT + sicDMFT.

III. PARAMAGNETIC SYSTEM

A. Stoichiometric compound

A basic characterization of the correlated electronic structure of paramagnetic (PM) NdNiO$_2$ was given in Ref. [18] for ambient temperatures, and in Ref. [19] for the lower-temperature regime. To set the stage, we here recapitulate the main findings and discuss the different site/orbital contributions within the correlated regime in some more detail.

On the DFT(LDA) level, the x^2–y^2 orbital has the lowest crystal-field level within the Ni($3d$) sector and the energy splittings to the other levels read $\{\varepsilon_{z^2}, \varepsilon_{x^2-y^2}, \varepsilon_{xz}, \varepsilon_{yz}, \varepsilon_{xy}\} = \{356, 0, 286, 286, 536\}$ meV. Then, in essence, the compound is a self-doped Mott insulator in DFT + sicDMFT, whereby the effectively Mott-insulating states are of half-filled Ni-$d_{x^2-y^2}$ kind and the self doping originates from a weakly

occupied band resulting from the hybridization between Nd($5d$) and Ni($3d$). Thus there is no Ni-$d_{x^2-y^2}$ quasiparticle dispersion crossing the Fermi level ε_{F} in the **k**-resolved spectral function, as shown in Fig. 2(a). At low energy, there are only SD-band-based electron pockets at Γ and A in the Brillouin zone.

Correspondingly, orbital weights along the given high-symmetry lines are provided in Figs. 2(b) to 2(f) for the most-relevant orbital sectors. The Ni-d_{z^2} contribution is twofold. First, it forms an incoherent part around -3 eV for $k_z = 0$, which becomes more coherent, flat, and intense in the $k_z = 1/2$ plane. Second, it has its prominent share in the SD-band formation for the Γ-pocket part. On the other hand, due to Mottness, the Ni-$d_{x^2-y^2}$ weight remains largely incoherent troughout the chosen **k**-space regions, with the exception of a small part along Z-R in the regime of the overall Ni-d_{z^2}-dominated spectrum. The Ni-t_{2g} $\{xz, yz, xy\}$ orbitals cause dispersing features between $[-3, -2]$ eV and have weak contribution to the SD band around A. The Nd($5d$)-based orbitals of z^2 and xy character are the main contributors to the SD band from the rare-earth site; Nd-d_{xy} for the A pocket and Nd-d_{z^2} pretty much everywhere else. The hybridization between Nd-d_{xy} and Ni-t_{2g} is also evident from the joint weight at deeper energies. The coupling between Ni-d_{z^2} and Nd-d_{z^2} is mostly confined to the Γ-X-M-Z path. Mott-insulating Ni-$d_{x^2-y^2}$ appears disconnected from the Nd($5d$)-Ni($3d$) hybridization, and indeed nearest-neighbor hopping from both relevant Nd($5d$) orbitals to the in-plane Ni-e_g orbital is zero [16,18,19]. The O($2p$) contribution is surely also vital in the given energy window, but a **k**-resolved discussion appears not highly instructive (see Ref. [18] for the **k**-integrated weight).

With high spectral-resolution focus on the low-energy region, a single-level feature at the Fermi level would become additionally visible for the here chosen lower temperature regime [19]. It stems from Ni-$d_{x^2-y^2}$ and is part of an intriguing Kondo(-lattice) mechanism, involving, furthermore, Ni-d_{z^2} and Nd-d_{z^2}. Basically, the Ni-d_{z^2} orbital mediates a Hund-assisted Kondo coupling between the d sectors of Ni and Nd, by enabling fluctuations between Ni-e_g and weakly correlated Nd-d_{z^2}.

B. Doped compound

Superconductivity in the nickelate thin films is reached by Sr doping [1], expected to introduce holes to the system. For completeness we here discuss both electron and hole doping within the VCA framework. From a preparation perspective, electron doping, e.g., by substituting Nd^{3+} by Ce^{4+}, should be more challenging [57]: the already delicate Ni$^+$ ionic state is reduced even further and the charge imbalance within the NiO$_2$ plane becomes additionally stretched. Indeed, the DFT + sicDMFT calculations show that the progress of the doping level δ toward the Ni($3d$) shell is strongly hindered on the electron-doped side [see Fig. 3(a)]. On the other hand, on the hole-doped side, the doping originating on the rare-earth site is nearly exclusively transferred to the Ni site. This furthermore underlines the weaker charge-transfer character compared to cuprates, where most holes reside on oxygen. The orbital-resolved filling of the Ni-e_g states with doping δ
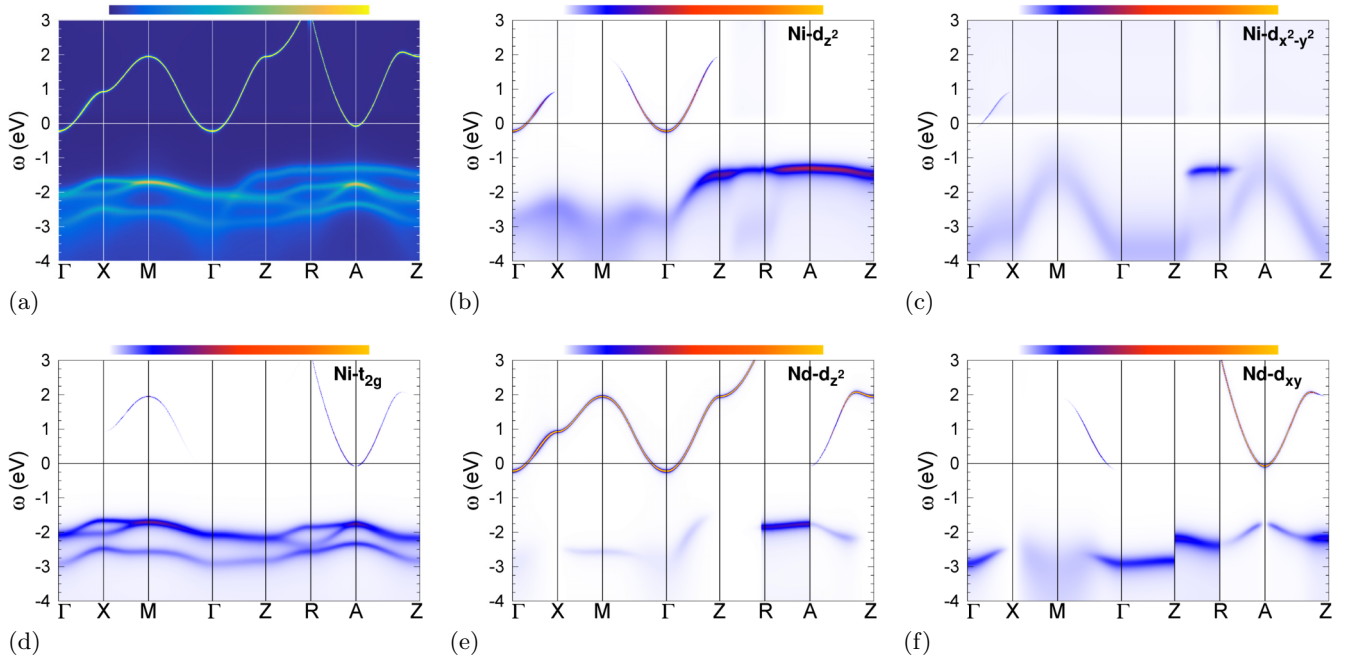
FIG. 2. Spectral information for pristine NdNiO$_2$. (a) **k**-resolved function $A(\mathbf{k}, \omega)$ along high-symmetry lines: Γ-X-M describes a triangle in the $k_z = 0$ plane and Z-R-A marks the same triangle translated to the $k_z = 1/2$ plane. Above the Fermi level, only the single SD dispersion is shown and further dispersions discarded in the plot. (b)–(f) **k**-resolved orbital weights (i.e., flat-bands) for the given spectral function: (b) Ni-d_{z^2}, (c) Ni-$d_{x^2-y^2}$, (d) Ni-t_{2g}, (e) Nd-d_{z^2}, and (f) Nd-d_{xy}. Note that with this chosen intensity resolution, the nondispersing-level feature at ε_F, giving rise to a Kondo(-lattice) mechanism [19] at lower T is not visible in $A(\mathbf{k}, \omega)$.

in Fig. 3(b) exhibits the strong hole attraction of Ni-d_{z^2} and its weaker additional electron filling on the electron-doped side. On the contrary, the Ni-$d_{x^2-y^2}$ filling is only weakly affected by the charge doping of the system and remains nearly inert. All these observations are in line with previous findings in a minimal-Hamiltonian description [19]. Note that the Ni-t_{2g} states are always close to complete filling throughout the
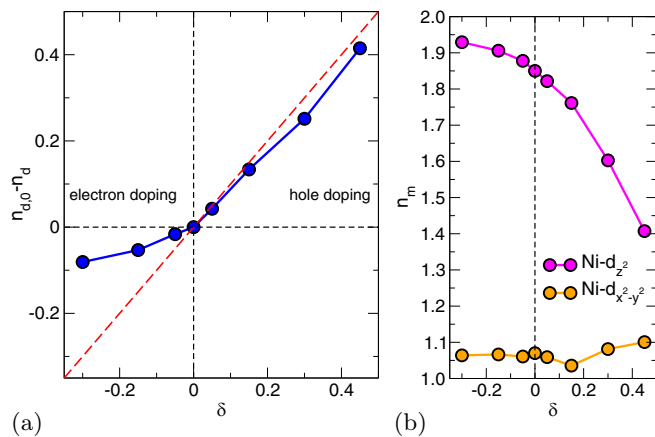

FIG. 3. Effective Ni(3d) occupation in doped NdNiO$_2$ from introducing δ holes/electrons. (a) Difference $n_{d,0}-n_d$ between the total occupation at $n_{d,0}$ zero doping and at given doping n_d, versus δ. The dashed red line marks the regime where the complete doping charge is transferred to Ni(3d). (b) Orbital-resolved filling of the Ni-e_g states.

doping landscape and seemingly do not play a key role for the phase diagram with δ.

We now turn to the **k**-resolved spectral evolution with doping, displayed in Fig. 4. Electron doping mainly leads to an expected downshift of the overall spectrum, resulting in an increased filling of the SD band. The Mott-insulating character of the Ni-$d_{x^2-y^2}$ orbital remains apparently robust, though the corresponding self-energy is considerably weakened with electron doping (cf. lower-left part of Fig. 5). Note, however, that this weakening proceeds even more strongly with hole doping (cf. lower-right part of Fig. 5), as observed already in the minimal-Hamiltonian picture [19]. It leads to a partial melting of the Ni-$d_{x^2-y^2}$-based Mott state for $\delta \geqslant 0.05$. Moreover, the SD electron pockets are shifted into the unoccupied region by a sizable amount already for $\delta = 0.05$. In line with this, the dominant Ni-d_{z^2} spectral part in the occupied region gets shifted progressively toward the Fermi level. The spectral evolution of the originally occupied Ni-d_{z^2} part is, in fact, one striking feature with hole doping. Its flat-band part in the $k_z = 1/2$ plane crosses ε_F here for $\delta \geqslant 0.15$.

Let us therefore pause with the further evolution to higher hole dopings for a moment and focus on the spectrum at $\delta = 0.15$ (cf. Fig. 6). The Ni-d_{z^2} flat-band part is touching the Fermi level [19,34] and the strength of the Ni-$d_{x^2-y^2}$ Mott state is weakened, giving rise to minor dispersive spectral weight at low energy. This Ni-$d_x^2 - y^2$ dispersive spectra is strongest close to the R point, where a van Hove singularity settles. The occupied Ni-t_{2g}, Nd-d_{z^2} and Nd-d_{xy} weights appear generally strengthened compared to the stoichiometric case. They are also shifted to lower energy, but do not partici-
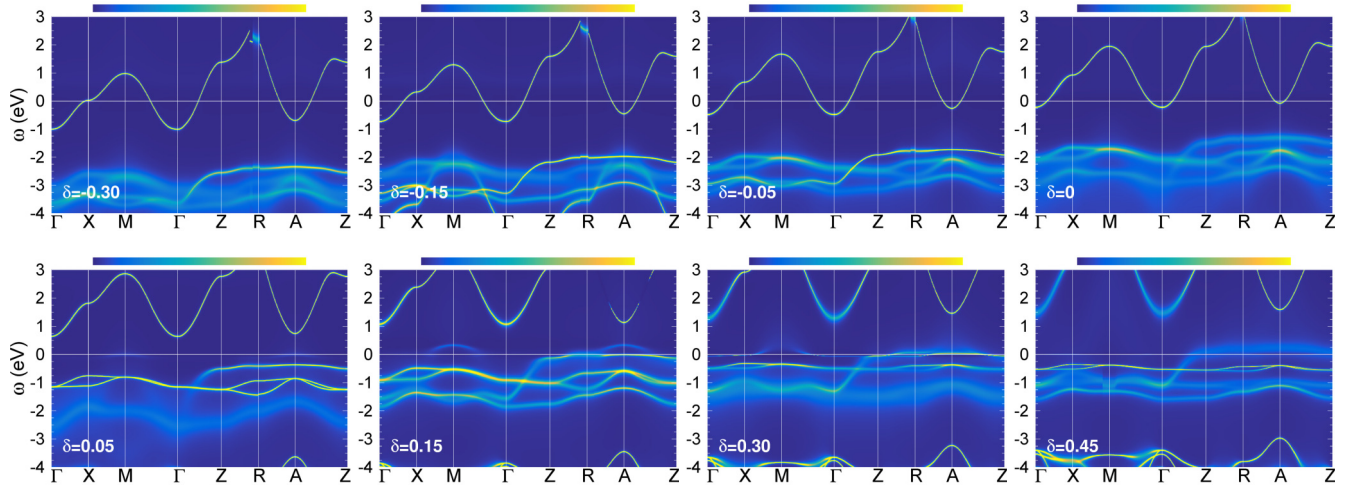
FIG. 4. Spectral function $A(\mathbf{k}, \omega)$ with doping δ. Top row, from left to right: $\delta = -0.30, -0.15, -0.05, 0$. Bottom row, from left to right: $\delta = 0.05, 0.15, 0.30, 0.45$. Same setting as in Fig. 2(a).

pate on the singular fermiology. The actual Fermi surface with obvious Ni-d_{z^2} weight at the A point is shown on the left of Fig. 6(g). Because of the flat-band character, the topology of the constant-energy surface changes quite significantly within a $\sim$100 meV range below ε_F. Going down in energy from $\omega = 0$, a hole surface around A transforms into an electron surface around Z. The substantial hole character just below the Fermi level is in line with experimental findings of hole-like transport in that doping region [7,8]. But note that the "actual" Fermi surface for a given $0.125 \lesssim \delta \lesssim 0.25$ in the region with low-T superconductivity is still very delicate, and perfect agreement between experiment and theory will be hard to reach. Nonetheless, we predict that the experimental $\delta = 0.15$ Fermi surface has the appearance of one of the three $\omega = [0, -0.045]$ eV plots of Fig. 6(g).
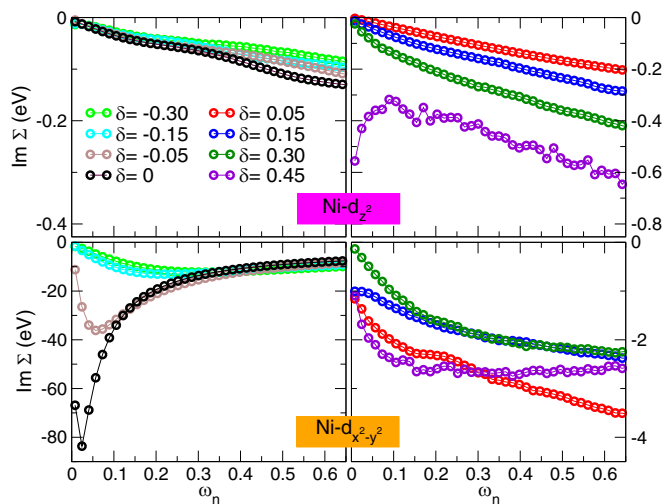

FIG. 5. Imaginary part Im $\Sigma(i\omega_n)$ of the Ni-e_g self energy on the Matsubara axis $\omega_n = (2n + 1)\pi T$ for different dopings δ. Top: Ni-d_{z^2} and bottom: Ni-$d_{x^2-y^2}$. Left part: $\delta = -0.30, -0.15, -0.05, 0$ and right part: $\delta = 0.05, 0.15, 0.30, 0.45$.

The Ni-e_g self-energies have a rather intriguing development with hole doping (cf. right part of Fig. 5). For Ni-d_{z^2}, the self-energy part Im $\Sigma(i\omega_n)$ grows with δ, and the low-frequency curvature increasingly departs from standard Fermi-liquid behavior. Fitting to the function $F = A \omega_n^\alpha$, the values α_δ read $\{\alpha_{0.05}, \alpha_{0.15}, \alpha_{0.40}\} = \{0.89, 0.74, 0.60\}$, while $\alpha = 1$ holds in a Fermi liquid. Furthermore for $\delta = 0.45$, the self-energy attains a negative curvature, signaling strong bad-metal/insulating tendencies. A clearly larger Ni-$d_{x^2-y^2}$ self-energy shows nearly zero curvature at $\delta = 0.15$, i.e., just when the Ni-d_{z^2} flat band starts to cross ε_F. Increasing hole doping further, first stabilizes a putative Fermi-liquid character with a low scattering rate [$\propto$ Im $\Sigma(0)$], but then jumps back to a high-scattering Mott-critical regime at $\delta = 0.45$. This data show that both Ni-e_g orbitals strongly affect each other in the hole-doped regime of NdNiO$_2$.

The development with hole doping can also be inspected from plotting the $\mathbf{k}$-integrated total spectrum and the local Ni-e_g spectrum at low energy in Fig. 7. The total spectrum around ε_F grows significantly for $\delta \geqslant 0.15$, but weakens again for $\delta = 0.45$. The low-energy Ni-e_g weight is small at stoichiometry; Ni-$d_{x^2-y^2}$ is essentially Mott insulating and Ni-d_{z^2} only weakly contributing based on its hybridization on the SD electron pockets. Those are shifted above the Fermi level for small hole doping, and hence only Ni-$d_{x^2-y^2}$ weight from a premelted Mott state appears close to ε_F. Once the flat band shifts into the low-energy region, the corresponding Ni-d_{z^2} weight starts to dominate the local spectrum. But it develops a pseudogap structure due to specific dispersion topology of a fully occupied(empty) flat branch below(above) the Fermi level. Note that the increased QP character of Ni-$d_{x^2-y^2}$ between entry and departure of the Ni-d_{z^2} flat-band part from the Fermi level becomes here also visible. As already derived from the self-energies, the high-doping region of the hole-doped side does not resemble a good metal. But its semimetallic/bad-metallic appearance is indeed in agreement with the weakly insulating behavior found in the experiment [7,8].
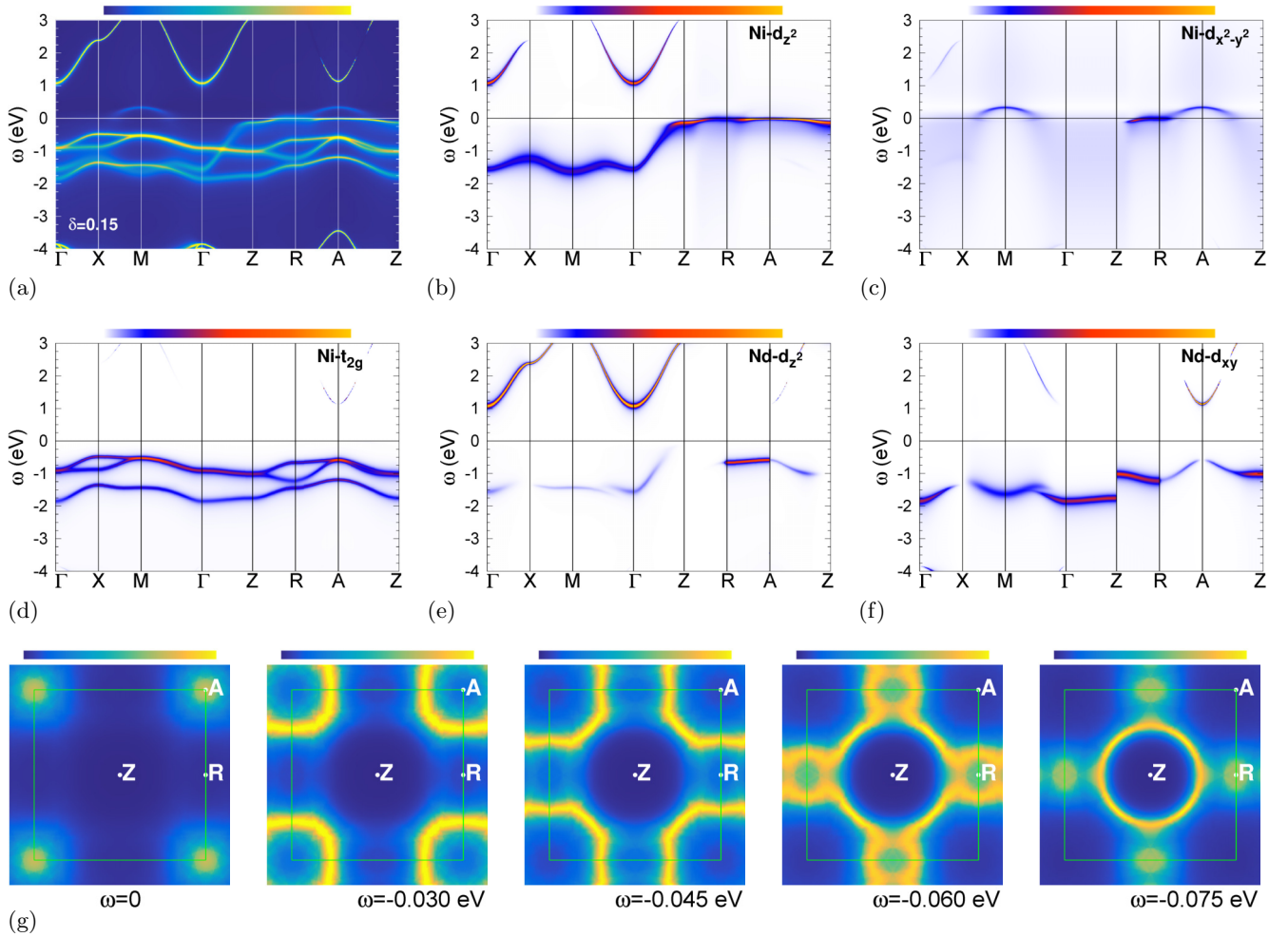
FIG. 6. Spectral information of hole-doped NdNiO$_2$ with $\delta = 0.15$. (a)–(f) As in Figs. 2(a) to 2(f). (g) Constant-energy surfaces in the $k_z = 1/2$ plane. Note that the maximum intensity for the surfaces in (g) is reduced by a factor of 3 compared to the one for $A(\mathbf{k}, \omega)$ in (a).

The filling scenario and **k**-space topology behind the Ni-d_{z^2} pseudogap structure for hole dopings beyond the superconducting region is one reason for weak metallicity, especially for in-plane transport, as already pointed out in Ref. [19]. However, in addition, the non-Fermi-liquid and heavily bad-metallic character of the Ni-d_{z^2}-dominated states, associated with the pseudogap structure and a specific Hund-metal scenario of Ni-e_g, is a second vital reason.

IV. ANTIFERROMAGNETIC SYSTEM

A key feature of structurally akin high-T_c cuprates is the prominent AFM phase at and near stoichiometry [58,59]. So far, static magnetic order in infinite-layer nickelates has been elusive in experiments, but the investigations point to a low-temperature behavior that deviates from straightforward paramagnetism [4–6].

From theory, there are various studies [9,17,28,33,60–67] that address ordered magnetism in these systems. In addition to more unlikely ferromagnetic (FM) order, the canonical orderings examined are G-type and C-type antiferromagnetism. While the G-AFM order displays antiparallel alignment be-

tween in-plane and c-axis nearest-neighbor (NN) Ni spins, the C-AFM order deviates therefrom in showing ferroalignment along the c-axis [see Figs. 8(a) and 8(b)]. Most results from DFT($+U$) and model-Hamiltonian DMFT calculations reveal a large ordered magnetic moment of $m_{\text{Ni}} \sim 1 \ \mu_B$ on the Ni site for these patterns. At stoichiometry, the C-AFM state appears energetically favorable against the nonmagnetic state and against FM order within DFT $+ U$ [33] and additionally against G-AFM when utilizing the SCAN (i.e., meta generalized-gradient approximation) functional in DFT [66]. However, note that electronic correlations are only treated on a static level in these approaches (e.g., there is no true PM state straightforwardly reachable), and furthermore they formally describe the system at $T = 0$. Nearest-neighbor in-plane exchange constants between Ni spins are estimated 65 meV [66] and 82 meV [65], i.e., roughly half the value usually revealed for high-T_c cuprates.

Here we report DFT + sicDMFT calculations for possible G-AFM and C-AFM ordering at $T = 30$ K. Two technical aspects have to be mentioned. First, the possible additional ordering of the Nd spins is not considered in this investigation. This is not unreasonable, as in most rare-earth compounds the corresponding $4f$-based spins order at much lower
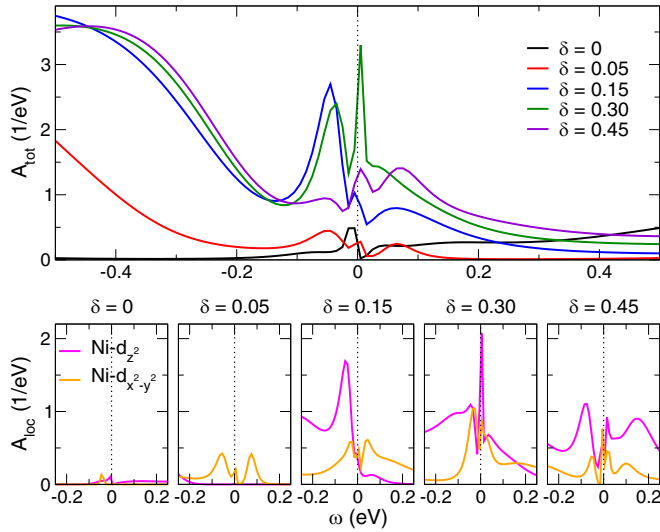
FIG. 7. Total spectral function after **k**-integration (top) and local Ni-e_g spectrum (bottom) of pristine and hole-doped NdNiO$_2$ at low energy.

temperature. Second, in a hybrid scheme of DFT and DMFT, there are, in principle, two basic formalisms to handle spin polarization: either it is treated both in the DFT *and* the DMFT part, or only on the DMFT level. The former approach includes ligand-based exchange mechanisms more directly,

but the T-independent exchange splitting from the DFT part usually ruins a reliable assessment of temperature effects. In other words, especially for transition-metal oxides, the robustness of the ordered magnetic moments with temperature is most often severely overestimated. Therefore, spin polarization is here treated only on the DMFT level, i.e., the Ni($3d$) self-energies beyond DFT are solely active in creating Ni ordered moments in the charge self-consistent computations. Note, however, that strictly speaking, the leaking of the Ni projected-local orbitals toward oxygen (cf. Fig. 1) gives rise to spin-polarization effects beyond pure Ni contributions. The magnetic order is initialized by starting from the converged PM state and using larger local magnetic fields on the given Ni sublattices in the first DFT + sicDMFT iteration.

The calculations are quite demanding and we so far did not succeed to stabilize a magnetically ordered phase in electron-doped NdNiO$_2$. At stoichiometry and with hole doping where this proves possible, the Ni magnetic moments turn out generally very small, with values $m_{Ni} \lesssim 0.1$ μ_B (see Table I). But importantly, the differentiation between an actual "zero moment" and such a small one is always very manageable from the present degree of convergence and accuracy. Though surprising in view of the Mott-insulating Ni-$d_{x^2-y^2}$ orbital with formally sizable local $S = 1/2$ spin at stoichiometry, Hayward and coworkers [4,68] noted from neutron scattering on polycrystalline bulk samples strong deviation from conventional $S = 1/2$ local-moment behavior
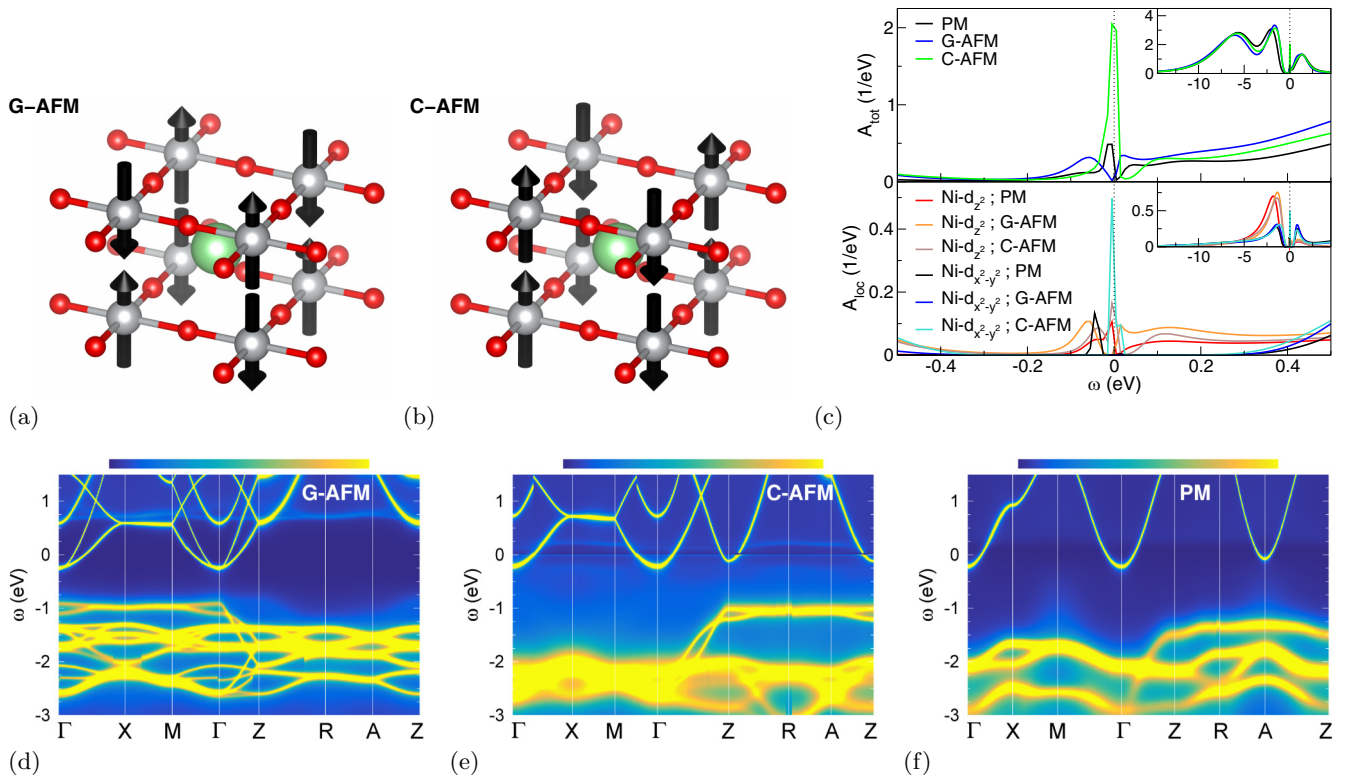

FIG. 8. Comparing PM and AFM-ordered NdNiO$_2$. (a) G-AFM ordering and (b) C-AFM ordering. (c) Total (top) and local Ni-e_g (bottom) spectral function for PM, G-AFM and C-AFM phase, respectively. (d)–(f) **k**-resolved spectral function along high symmetry lines for the (d) G-AFM, (e) C-AFM, and (f) PM phases. The $\sqrt{2} \times \sqrt{2}$ enlarged in-plane unit cell translates into $X \leftrightarrow M$ and $R \leftrightarrow A$ for the (G,C)-AFM structure. And the upper Ni-d_{z^2} flat-band part is flipped with respect to k_z for the G-AFM structure due to the doubled unit cell along c.

TABLE I. Ordered Ni magnetic moment in the G-AFM and C-AFM phase at $T = 30$ K and energy difference to the PM phase.

| Magnetic order | $m_{\mathrm{Ni}}\,(\mu_{\mathrm{B}})\,,\,E_{\mathrm{tot}}^{\mathrm{AFM}} - E_{\mathrm{tot}}^{\mathrm{PM}}$ (meV/atom) | |
	$\delta = 0$	$\delta = 0.15$
G-AFM	0.076 , 105	0.059 , 126
C-AFM	0.081 , 20	0.000 , –

of Curie-Weiss form. In Ref. [4], the data analysis are performed by assuming G-AFM order with a sensitivity limit of 0.06 μ_{B}/Ni.

In the present investigation, supercells of $\sqrt{2} \times \sqrt{2} \times 1$ kind for the C-AFM and of $\sqrt{2} \times \sqrt{2} \times 2$ for the G-AFM structure are utilized. At stoichiometry, the PM phase has the lowest total energy for the given temperature. But the energy difference $\Delta E = 20$ meV/atom to the C-AFM phase is rather small, whereas the G-AFM phase with $\Delta E = 105$ meV/atom does not appear as a relevant competitor. For these three different phases, Fig. 8(c) displays total and local Ni-e_g spectral functions, and Figs. 8(d) to 8(f) exhibit the corresponding **k**-resolved spectra. Inspection of the total spectrum renders it obvious that, though the ordered moments are tiny, intriguingly, the low-energy spectra of the different magnetic phases are actually quite different. Compared to the PM phase, the small peak just below the Fermi level is substantially enhanced in the C-AFM phase and more or less suppressed for the G-AFM phase. However, all three phases still display the SD electron pockets at the Fermi level. The key difference between the G-AFM and C-AFM low-energy physics is the enhancement of the Ni-$d_{x^2-y^2}$ single-level feature at ε_{F} for the latter phase. This becomes clear from the cyan curve in the lower panel of Fig. 8(c), as well as from the nondispersive feature in $A(\mathbf{k}, \omega)$ at the Fermi level in Fig. 8(e). That Kondo(-lattice) resonance exists also in the PM phase [19], yet with reduced weight [and therefore not visible within the given resolution in Fig. 8(e)]. The C-AFM phase may thus be interpreted as an exotic phase with coexistence of antiferromagnetic ordering and Kondo(-lattice) screening [69–72]. Because of the weak filling of the SD band, the latter Kondo physics takes place in an underscreening scenario, leaving room for magnetic ordering. Additionally, since the Kondo screening is mainly mediated by the d_{z^2} orbitals of Ni and Nd [19], the ferroalignment of spins along the c-axis in the C-AFM phase enables a screening action without additional spin flip. This may explain as to why the G-AFM phase cannot easily coexist with Kondo screening.

For finite hole doping $\delta = 0.15$, the C-AFM phase has transformed into the PM phase with zero ordered Ni moment. On the contrary, the G-AFM phase still remains (meta)stable with somewhat reduced m_{Ni} compared to $\delta = 0$ (see Table I). Notably, as the SD pockets are shifted above the Fermi level for that hole-doping level, partial Kondo screening of the pristine-scenario kind has vanished. Figure 9 shows that close to the Fermi level, the Ni-d_{z^2} character is enhanced and the Ni-$d_{x^2-y^2}$ one suppressed in the doped G-AFM phase compared to the PM phase. Though energetically less favorable (see Table I), if NN-AFM ordering is indeed stable at low temperature and with doping, there would be a δ-induced
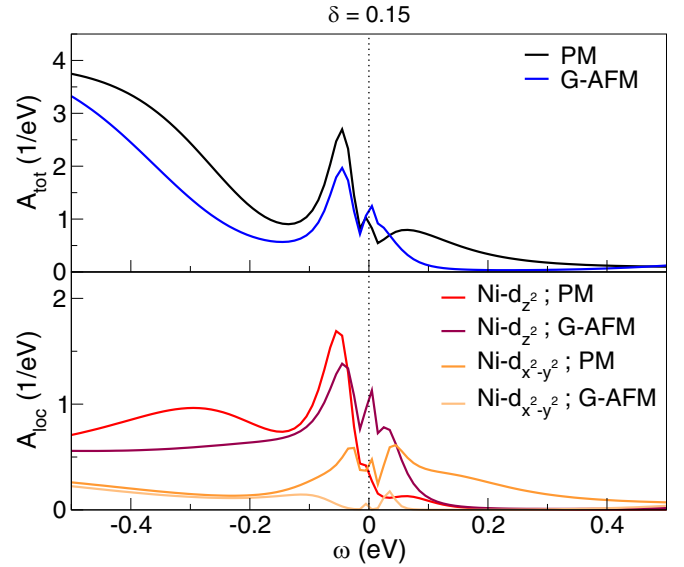

FIG. 9. Comparison of PM and G-AFM low-energy spectral functions at doping level $\delta = 0.15$. (Top) Total spectrum and (bottom) local Ni-e_g spectrum.

transition from C-AFM to G-AFM ordering. Note that a qualitative change of magnetic order with doping has also been deduced by Leonov and Savrasov [64] from DFT + DMFT calculations for the system at ambient temperature, albeit differently with G-AFM order at stoichiometry and C-AFM order at finite hole doping.

V. IMPACT OF METHOD-BASED CHOICES

Before summarizing and discussing the physical content of the obtained results, let us weigh the influence of the performed choices within the DFT + sicDMFT scheme onto the present findings.

Concerning the Coulomb interactions on Ni and O, the compatibility of the given Ni($3d$) onsite Hubbard U and Hund's exchange J_{H} together with the present SIC configuration in view of describing the main NdNiO$_2$ transport characteristics was already discussed in Ref. [18]. The decisive impact of the SIC from the oxygen sites in substantially enhancing the system correlation strength is reported in Appendix A. A somewhat smaller U value for Ni($3d$) of $U = 7$–9 eV would therefore not change the key findings by qualitative means. A smaller J_{H} would weaken the shifting of the Ni-d_{z^2} flat-band part toward the Fermi level with hole doping, as the associated local Ni-e_g $S = 1$ state has to work harder against the crystal field [65].

We did not explicitly employ local Coulomb interactions beyond the DFT treatment on the Nd site. First, such terms are believed to be significantly weaker than for Ni($3d$), and the Nd($5d$) filling is furthermore comparatively small. Second, the present choice of the correlated subspace with encompassing the 12 mainly Ni-O-dominated KS states as projection sphere, carries only minor explicit Nd($5d$) orbital weight. The body of Nd($5d$) character is associated with higher-lying KS states in the unoccupied part of the spectrum [18]. To check the possible influence of Nd($5d$) interactions, we therefore

increased the KS projection sphere to 18 states and introduced an additional local Slater Hamiltonian on the Nd site with $U_{Nd} = 3$ eV and $J_{H,Nd} = 0.3$ eV solved within a now two-impurity DFT + sicDMFT cycle (while keeping interactions on Ni and SIC treatment for O unaltered). Note that this enlarged number of KS states becomes then very similar to the projection window utilized, e.g., by Karp *et al.* [24,73]. In this stronger atomic-orbital picture of Ni($3d$) states, the Ni-d_{z^2} turns out significantly *lower filled* than in the stronger crystal-orbital 12-KS-state projection [74] because of associated orbital weight in the higher *unoccupied* region [18]. The overall physics at stoichiometry and with hole doping does not change qualitatively in DFT + sicDMFT employing the 18-KS-state projection. However, already at stoichiometry, the occupied Ni-d_{z^2} flat band in the $k_z = 1/2$ part of reciprocal space is located much closer to the Fermi level. And for hole doping $\delta = 0.15$, most of this flat-band part has yet crossed ε_F. Note that within the combination of DFT and DMFT, there is no unique criterion to design the correlated subspace and thus to per se favor either of both KS projection spheres based on formal grounds. Based on our physical understanding, employing the 12-KS-state projection is closer to the generic Hubbard-model construction idea, realizing a stronger Wannier(-like) picture for Ni($3d$), with a more stringent orbital-to-band resemblance. In addition, high-lying KS states are less well defined than occupied/low-lying ones since the Hohenberg-Kohn principles deal with the occupied charge density. Therefore, artifacts or basis-dependent issues are more likely for high-energy unoccupied KS states.

Compared to the experiment, the here-revealed behavior with hole doping does not seem perfectly commensurable with the experimental phase diagram. There, the superconducting region stretches from $0.125 \lesssim \delta \lesssim 0.25$, whereas the prominent role of Ni-d_{z^2} seemingly peaks here at $\delta = 0.30$. There may be several reasons for this difference. First, due to our sparse doping sampling, a "true" peaking Ni-d_{z^2} behavior within the experimental superconducting doping range is still possible, as for $\delta = 0.30$ there is already the pseudogap onset. Second, we only assume $\delta = x$ to hold, but since the present VCA approach has its limitations, a small shift of behavior would not be surprising. Moreover, throughout the study, the stoichiometric lattice parameters are employed, and the c-axis increase with hole doping [1] is not included in the calculations. And third, albeit the Ni-d_{z^2} flat-band neighborhood to the Fermi level is believed to be the key driving force for superconductivity, its ε_F entry and departure points do not necessarily have to agree exactly with the phase boundaries for superconductivity.

The hybrid treatment, selection, and initialization of magnetic order allows for alternatives. A different initialization protocol, i.e., starting from a self-consistent constrained-field or Hartree-Fock solution, could possibly lead to the (meta)stabilization of larger-moment phases. Long-range ordering wave vectors beyond C- and G-AFM might be (meta)stabilized in extended considerations, which is, however, beyond the scope of this work.

Finally, the present status of the DFT + (sic)DMFT method asks for certain choices and the final outcome does not only depend on pure convergence parameters as in nowadays practical DFT. This may be seen as a drawback, but it emphasizes the complexity of the interacting many-body problem and leaves room for physical intuition, which has ever been a key aspect when pushing the frontiers of condensed matter.

VI. SUMMARY AND DISCUSSION

The present DFT + sicDMFT study of pristine and doped NdNiO$_2$ uncovers two key results. First, the character of the paramagnetic electronic structure changes distinctively with doping. On the electron-doped side, which may be challenging to explore experimentally, the nickelate is a (Ni,Nd)-d_{z^2} based one-band system in a Mott-critical background of Ni-$d_{x^2-y^2}$ kind. At stoichiometry, the later background is of robust Mott-insulating nature and the solid one-band part at the Fermi energy has evolved into a weakly filled self-doping entity. Since the SD dispersion carries relevant Ni-d_{z^2} itinerancy, one may also picture this phase as of orbital-selective type, eventually decorated with partial Kondo screening at low temperature [19]. Already small hole doping leads to a sizable upward shift of the SD band into the unoccupied region, and the stabilization of a Ni-$d_{x^2-y^2}$-based weakly doped/premelted Mott-insulator in which Ni-d_{z^2} degrees of freedom are frozen. For hole doping $\delta \gtrsim 0.15$, the Ni-d_{z^2} flat-band part in the $k_z = 1/2$ region crosses the Fermi level and the system displays intriguing {Ni $- d_{z^2}$, Ni-$d_{x^2-y^2}$} physics at low energy. As a result thereof, unconventional superconductivity sets in at low temperature. For even larger hole doping $\delta > 0.30$, the nickelate does not attain a conventional Fermi-liquid state, but enters a pseudogap and a bad Hund-metal regime. In other words, the two-orbital Ni-e_g subspace with filling $n_{e_g} \sim 2.5$ becomes strongly correlated with vanishing coherence scale due to the interplay of the Hund's J_H with the remaining local Coulomb interactions in the Ni($3d$) and O($2p$) shells. Take notice that other recent theoretical works mark general Nd$_{1-x}$Sr$_x$NiO$_2$ as a Hund metal, and suggest similarities with iron-pnictide physics [35,36]. However, from our point of view, the (near) Mott-insulating state of Ni-$d_{x^2-y^2}$ and large filling of Ni-d_{z^2} close to stoichiometry render this somewhat questionable. As described above, strong Hund-metal physics occurs here only for larger hole dopings, and therefore loosely speaking, superconductivity in doped NdNiO$_2$ appears to take place when "cuprates" (from the underdoped side) and "pnictides" (from the overdoped side) meet and bind together through a flat-band scenario.

Second, it is shown that magnetic order of AFM type may be a vital competitor with and without doping at low-enough temperatures, albeit the associated features are far from those of conventional antiferromagnetism in, e.g., stoichiometric high-T_c cuprates. At $T = 30$ K, the ordered Ni moments are already very small for all encountered cases, which either points to a critical temperature in the same range or to strong quantum fluctuations/screening. The size of the local moment surely also depends on calculational settings, e.g., on the method to handle spin-symmetry breaking in realistic DMFT and the choice of the correlated subspace. But the present choices are believed physically sound, and therefore the general outcome of significantly reduced Ni moments around

$T = 30$ K should be qualitatively robust. The C-AFM phase is energetically more favorable than the G-AFM phase at stoichiometry, obviously benefiting from a coexistence with partial Kondo screening. This result sounds rather exotic for a TM(3d) oxide, however, the experimental searches for magnetic order in infinite-layer nickelates also point to singular low-T behavior [4–6]. Furthermore, we here detect an apparent transition from C-AFM to G-AFM order/correlations with hole doping. This would be coherent with the fact that the Kondo-screening tendencies at stoichiometry vanish with hole doping because of the shift of the SD band above the Fermi level.

This work complements our previous investigation for infinite-layer nickelates [18,19]. It is worthwhile to note that the obtained essential picture of relevant Ni multiorbital physics, and especially the importance of the Ni-d_{z^2} flat-band part for hole dopings in the superconducting region, is very robust across these studies. For instance, three different frameworks to describe the doped NdNiO$_2$ compound, i.e., supercell with impurities [18], minimal Hamiltonian with chemical-potential shift [19], and eventually the present VCA approach, all lead to the same qualitative result. Thereby, the role of explicit Coulomb interactions on oxygen is not of "decorative" type, but truly decisive for the revealed physics (see the Appendix for further details). When abandoning the SIC inclusion into the theoretical framework and employing conventional DFT + DMFT calculations, the Ni-d_{z^2} flat-band part remains well below the Fermi level for the relevant dopings, in agreement with comparable studies of this type [22,35,64,73]. Moreover, a recent GW + EDMFT investigation of Petocchi *et al.* [34], which also included beyond-Ni(3d)-based correlations, supports our picture.

Let us finally take the opportunity to selectively touch base with further theoretical studies from other research groups. In DFT + U studies by Choi *et al.* [33], the C-AFM order also turns out to be a proper candidate for magnetism in NdNiO$_2$. Furthermore, notably at stoichiometry, the Ni-d_{z^2} flat-band part in the $k_z = 1/2$ region is placed right at the Fermi level for this order within the given static-correlation scheme (see also Appendix B). Though at a first glance looking quite different to our result for the C-AFM phase [compare with Fig. 8(e)], this outcome could carry similar physics. The DFT + U scheme may mimic Kondo(-like) physics by placing a spin-resolved flat band right at the Fermi level. In this way, the corresponding (local) spin becomes highly susceptible, and that is more or less the best a static-correlation scheme may achieve for Kondo-based spin fluctuations. The fact that this band is of dominant Ni-d_{z^2} character underlines our previous finding of the crucial Ni-d_{z^2} role in mediating Kondo-screening in NdNiO$_2$ [19]. However, this DFT + U result for Ni-d_{z^2} *at stoichiometry* should not be directly related to the DFT + sicDMFT result of the Ni-d_{z^2} flat-band part crossing the Fermi level with *sizable hole doping*.

In a different DFT + U assessment by Liu *et al.* [63], the G-AFM order is found to be stable at stoichiometry, but the Ni magnetic moment and the general AFM ordering is also easily weakened by the impact of the SD band. The resistivity upturn below $T \sim 70$ K is associated with the transition into this bad-AFM metal when lowering temperature from the PM phase. Although the details differ, that bad-AFM

metal regime could resemble our AFM plus Kondo-screening phase.

Finally, all our theoretical studies on the thin-film NdNiO$_2$ system, i.e., Refs. [18,19] and this one, are conducted in a "bulk-like" fashion by using the thin-film lattice parameters for a bulk-crystal calculation. Already several works [75–78] addressed the explicit thin-film geometry on a SrTiO$_3$ substrate via supercell DFT(+U) calculations. However, while nickelate/SrTiO$_3$ interface physics may have some impact, from the comparison of the currently available experimental data and the results of a theoretical bulk-like approach there is no pressing evidence that key effects are missing in the latter. Furthermore, the experimental thin films with ∼10 nm thickness are rather bulky, accounting for more than 30 vertical unit cells. The measured critical current densities [2] of more than 300 kA/cm^2 would also be quite large for sole two-dimensional superconductivity in the interface. Nonetheless, investigating NdNiO$_2$ in an ultrathin limit of only a few unit cells would surely be interesting.

In the end, different theoretical concepts for infinite-layer nickelates are presently put to the test (see, e.g., Ref. [79] for a recent review). Ultimately, only experiment can tell which of these concepts is closest to the truth. The here-presented evolution of the doping-dependent phenomenology is already in line with various experimental findings [7,8,10], most notably concerning the identification of weakly insulating regions on either side of the superconducting doping region as well as the dominance of hole-like transport for $\delta > 0.15$. In a next step, angle-resolved photoemission spectroscopy (ARPES) measurements appear deciding since therefrom the correlation strength and the fate of the Ni-d_{z^2} flat-band part with doping is most clearly revealed. But ARPES on these thin film architectures, together with the necessary resolution for possible flat-band physics out of the $k_z = 0$ plane, is surely demanding. By any means, the infinite-layer nickelate physics is highly puzzling and appears to integrate various condensed-matter regimes into one materials class, providing room for intense research in the future.

APPENDIX A: ROLE OF EXPLICIT COULOMB INTERACTIONS ON OXYGEN

As discussed in more detail in Ref. [39], the SIC treatment for most relevant O(2p) in the present form effectively introduces a U_{pp} and a U_{pd} interaction term. As a result, the pd-splitting between O(2p) and Ni(3d) is enhanced compared to LDA, and the hoppings t_{pd} between those site-orbitals are renormalized. To assess the effect of including explicit Coulomb interactions on oxygen via a SIC-modified O pseudopotential, we perform also calculations within the conventional DFT + DMFT scheme for the paramagnetic
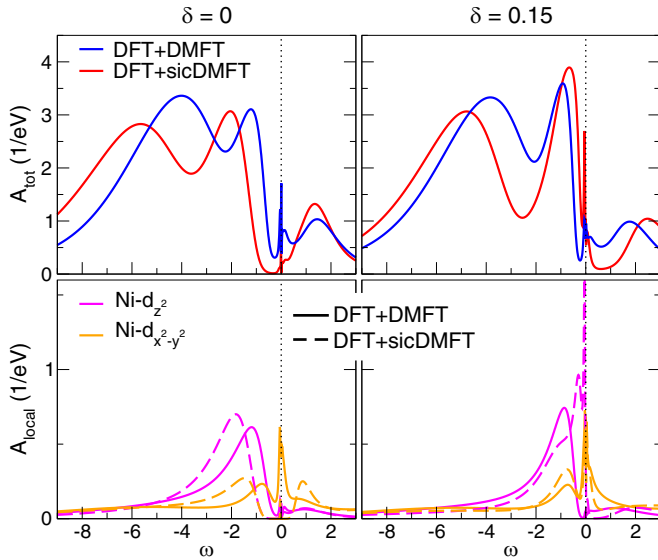
FIG. 10. Comparison of DFT + DMFT and DFT + sicDMFT spectral functions for pristine NdNiO$_2$ (left) and at doping level $\delta = 0.15$ (right). (Top) Total spectrum and (bottom) local Ni-e_g spectrum.

system. There, the standard O pseudopotential based on LDA is employed.

In Fig. 10, the total spectral function $A_{\text{tot}}(\omega)$ and the local Ni-e_g part are shown in comparison for both computational schemes. One may infer that though the Hubbard U on the Ni site is identical, the overall correlation strength in the standard DFT + DMFT approach is much weaker than with including additionally Coulomb interactions on oxygen. At stoichiometry, the system is a strongly renormalized metal, i.e., with Ni-$d_{x^2-y^2}$ not reaching a Mott-insulating state, in line with other works [22,35,73]. This can be explained by the fact that an effective treatment of U_{pp} and U_{pd} is missing in conventional DFT + DMFT. Thus a sole focus on the Hubbard U on Ni to assess the correlation strength in infinite-layer nickelates may be misleading since a vital contribution is carried by the Coulomb interactions on and from oxygen because of the late-TM-oxide context. Furthermore, the distance between oxygen and Ni(3d) states, associated with both main peaks in the respective total spectrum, is somewhat larger from the DFT + sicDMFT calculations, which reflects the increase of pd splitting.

For the hole-doped compound, it is additionally seen that the Ni-d_{z^2} character does not show a peak close to the Fermi level for DFT + DMFT. This is understood from Fig. 11, which displays the comparison between DFT + sicDMFT and DFT + DMFT on the level of the **k**-resolved spectral function $A(\mathbf{k}, \omega)$ as well as the imaginary part of the Ni-e_g self-energy $\text{Im}\,\Sigma(i\omega_n)$. It becomes obvious that the previously discussed key effect of hole doping, namely the shift of the Ni-d_{z^2} flat-band part in the $k_z = 1/2$ plane is missing in DFT + DMFT. Moreover, the SD electron pockets are much weaker shifted to higher (unoccupied) energies, also in line with previous DFT + DMFT studies [22,35,64,73]. This difference in doping evolution of those specific dispersions has to be related to the fact that both individual Ni-e_g orbitals hybridize very differently with O(2p) (see last paragraph in
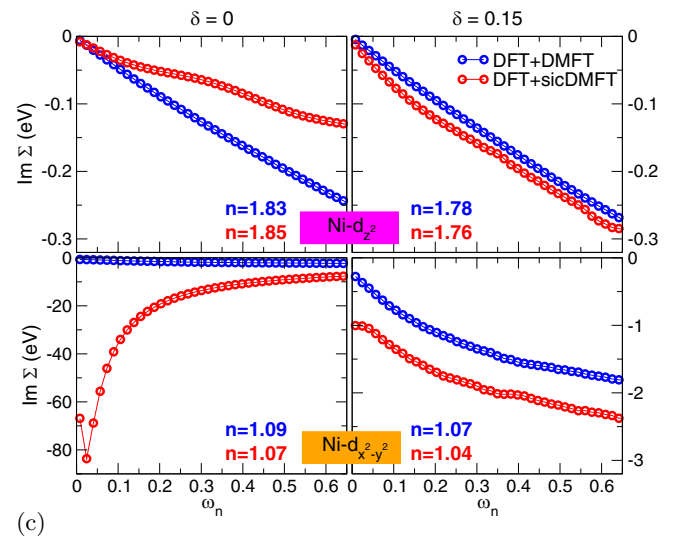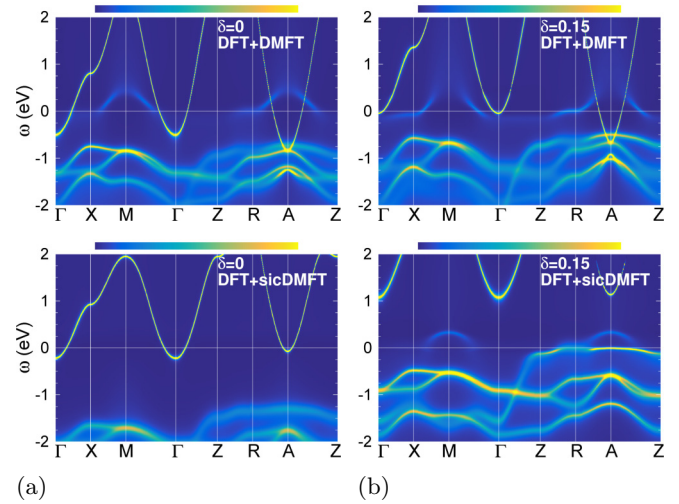

FIG. 11. Comparison between DFT + DMFT and DFT + sicDMFT for pristine (left) and $\delta = 0.15$ hole-doped (right) NdNiO$_2$. (a) **k**-resolved spectral function $A(\mathbf{k}, \omega)$ and (b) imaginary part of the Ni-e_g self-energy $\text{Im}\,\Sigma(i\omega_n)$.

Sec. II). Consequently, the Ni-$d_{x^2-y^2}$ self-energy at $\delta = 0.15$ also does not show a clear low-frequency anomaly in DFT + DMFT since that one should be linked to the Ni-d_{z^2} flat-band part residing at ε_F. However, note that the Ni-e_g occupations up to $\delta = 0.15$ do not seem to differ strongly between both correlation schemes.

In summary, there are strong qualitative differences between the DFT + DMFT and the DFT + sicDMFT description of pristine and doped NdNiO$_2$, which ask for a rethinking of the sole TM-driven correlation picture of late transition-metal oxides in many numerical approaches.

APPENDIX B: DFT + sicU RESULT FOR THE C-AFM PHASE

For comparison, we plot in Fig. 12 the band structures obtained within DFT + U and DFT + sic$U$ for the C-AFM phase. The DFT + sic$U$ scheme amounts to the
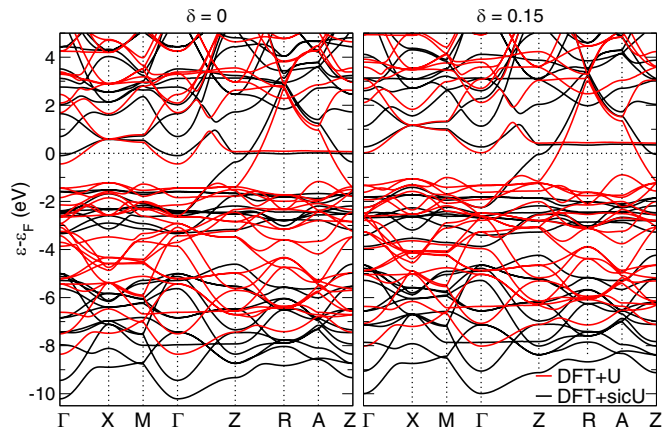
FIG. 12. Comparison between the DFT + U (red) and DFT + sicU band structure for pristine (left) and $\delta = 0.15$ hole-doped (right) NdNiO$_2$ in the C-AFM phase.

conventional DFT + U framework, but here employing the SIC-modified oxygen pseudopotential. It hence mirrors the DFT + sicDMFT scheme for a Hartree-Fock-like treatment of electronic correlations. Note, however, that the correlated subspace in this standard implementation of DFT + U is defined by projecting all KS bands onto the Ni(3d) cubic harmonics, as done in most available electronic structure codes. A Hubbard $U = 5$ eV and $J_H = 1$ eV is utilized in line with values used in other DFT + U studies of NdNiO$_2$ [9,28,33]. No Hubbard interactions are used on the Nd site.

We confirm the flat-band behavior in the $k_z = 1/2$ region already at stoichiometry, as described in Refs. [33,66]. This result holds with the inclusion of SIC on oxygen, but further renormalization of the electron pockets takes place close to the Fermi level. The wide band crossing the Fermi level along Z-R is of dominant Ni-$d_{xz,yz}$ and Nd-d_{xy} character. At higher occupied energies, the pd splitting is increased as expected from the SIC inclusion [18]. Note that a sizable downward shift of the O(2p) states is also obtained from GW calculations [80]. With hole doping, the electron pockets become depleted and the flat-band part is also shifted above the Fermi level. The Ni AFM moments are sizable and read $m_{Ni} = \pm 1.1(1.0)\,\mu_B$ without(with) inclusion of SIC, and are even slightly growing in size with hole doping.

[1] D. Li, K. Lee, B. Y. Wang, M. Osada, S. Crossley, H. R. Lee, Y. Cui, Y. Hikita, and H. Hwang, Nature **572**, 624 (2019).

[2] M. Osada, B. Y. Wang, B. H. Goodge, K. Lee, H. Yoon, K. Sakuma, D. Li, M. Miura, L. F. Kourkoutis, and H. Y. Hwang, Nano Lett. **20**, 5735 (2020).

[3] M. Osada, B. Y. Wang, K. Lee, D. Li, and H. Y. Hwang, Phys. Rev. Mater. **4**, 121801(R) (2020).

[4] M. A. Hayward and M. J. Rosseinsky, Solid State Sci. **5**, 839 (2003).

[5] B.-X. Wang, H. Zheng, E. Krivyakina, O. Chmaissem, P. P. Lopes, J. W. Lynn, L. C. Gallington, Y. Ren, S. Rosenkranz, J. F. Mitchell, and D. Phelan, Phys. Rev. Mater. **4**, 084409 (2020).

[6] Y. Cui, C. Li, Q. Li, X. Zhu, Z. Hu, Y. feng Yang, J. S. Zhang, R. Yu, H.-H. Wen, and W. Yu, arXiv:2011.09610.

[7] D. Li, B. Y. Wang, K. Lee, S. P. Harvey, M. Osada, B. H. Goodge, L. F. Kourkoutis, and H. Y. Hwang, Phys. Rev. Lett. **125**, 027001 (2020).

[8] S. Zeng, C. S. Tang, X. Yin, C. Li, M. Li, Z. Huang, J. Hu, W. Liu, G. J. Omar, H. Jani, Z. S. Lim, K. Han, D. Wan, P. Yang, S. J. Pennycook, A. T. S. Wee, and A. Ariando, Phys. Rev. Lett. **125**, 147003 (2020).

[9] M. Hepting, D. Li, C. J. Jia, H. Lu, E. Paris, Y. Tseng, X. Feng, M. Osada, E. Been, Y. Hikita, Y. D. Chuang, Z. Hussain, K. J. Zhou, A. Nag, M. Garcia-Fernandez, M. Rossi, H. Y. Huang, D. J. Huang, Z. X. Shen, T. Schmitt, H. Y. Hwang, B. Moritz, J. Zaanen, T. P. Devereaux, and W. S. Lee, Nat. Mater. **19**, 381 (2020).

[10] B. H. Goodge, D. Li, M. Osada, B. Y. Wang, K. Lee, G. A. Sawatzky, H. Y. Hwang, and L. F. Kourkoutis, Proc. Natl. Acad. Sci. U.S.A. **118**, e2007683118 (2021).

[11] M. Rossi, H. Lu, A. Nag, D. Li, M. Osada, K. Lee, B. Y. Wang, S. Agrestini, M. Garcia-Fernandez, Y. D. Chuang, Z. X. Shen, H. Y. Hwang, B. Moritz, K.-J. Zhou, T. P. Devereaux, and W. S. Lee, arXiv:2011.00595.

[12] Y. Xiang, Q. Li, Y. Li, H. Yang, Y. Nie, and H.-H. Wen, Chin. Phys. Lett. **38**, 047401 (2021).

[13] B. Y. Wang, D. Li, B. H. Goodge, K. Lee, M. Osada, S. P. Harvey, L. F. Kourkoutis, M. R. Beasley, and H. Y. Hwang, Nat. Phys. **17**, 473 (2021).

[14] Q. Gu, Y. Li, S. Wan, H. Li, W. Guo, H. Yang, Q. Li, X. Zhu, X. Pan, Y. Nie, and H.-H. Wen, Nat Commun **11**, 6027 (2020).

[15] X. Wu, D. Di Sante, T. Schwemmer, W. Hanke, H. Y. Hwang, S. Raghu, and R. Thomale, Phys. Rev. B **101**, 060504(R) (2020).

[16] Y. Nomura, M. Hirayama, T. Tadano, Y. Yoshimoto, K. Nakamura, and R. Arita, Phys. Rev. B **100**, 205138 (2019).

[17] A. S. Botana and M. R. Norman, Phys. Rev. X **10**, 011024 (2020).

[18] F. Lechermann, Phys. Rev. B **101**, 081110(R) (2020).

[19] F. Lechermann, Phys. Rev. X **10**, 041002 (2020).

[20] M. Jiang, M. Berciu, and G. A. Sawatzky, Phys. Rev. Lett. **124**, 207004 (2020).

[21] G.-M. Zhang, Y.-F. Yang, and F.-C. Zhang, Phys. Rev. B **101**, 020501(R) (2020).

[22] L. Si, W. Xiao, J. Kaufmann, J. M. Tomczak, Y. Lu, Z. Zhong, and K. Held, Phys. Rev. Lett. **124**, 166402 (2020).

[23] M. Kitatani, L. Si, O. Janson, R. Arita, Z. Zhong, and K. Held, npj Quantum Mater. **5**, 59 (2020).

[24] J. Karp, A. S. Botana, M. R. Norman, H. Park, M. Zingl, and A. Millis, Phys. Rev. X **10**, 021061 (2020).

[25] P. Adhikary, S. Bandyopadhyay, T. Das, I. Dasgupta, and T. Saha-Dasgupta, Phys. Rev. B **102**, 100501(R) (2020).

[26] Z.-J. Lang, R. Jiang, and W. Ku, arXiv:2005.00022.

[27] E. Been, W.-S. Lee, H. Y. Hwang, Y. Cui, J. Zaanen, T. Devereaux, B. Moritz, and C. Jia, Phys. Rev. X **11**, 011050 (2021).

[28] K.-W. Lee and W. E. Pickett, Phys. Rev. B **70**, 165109 (2004).

[29] L.-H. Hu and C. Wu, Phys. Rev. Research **1**, 032046(R) (2019).

[30] Y.-H. Zhang and A. Vishwanath, Phys. Rev. Research **2**, 023112 (2020).

[31] P. Werner and S. Hoshino, Phys. Rev. B **101**, 041104(R) (2020).

[32] J. Chang, J. Zhao, and Y. Ding, Eur. Phys. J. B **93**, 220 (2020).

[33] M.-Y. Choi, W. E. Pickett, and K.-W. Lee, Phys. Rev. Research **2**, 033445 (2020).

[34] F. Petocchi, V. Christiansson, F. Nilsson, F. Aryasetiawan, and P. Werner, Phys. Rev. X **10**, 041047 (2020).

[35] Y. Wang, C.-J. Kang, H. Miao, and G. Kotliar, Phys. Rev. B **102**, 161118(R) (2020).

[36] B. Kang, C. Melnick, P. Semon, G. Kotliar, and S. Choi, arXiv:2007.14610.

[37] S. Y. Savrasov, G. Kotliar, and E. Abrahams, Nature **410**, 793 (2001).

[38] D. Grieger, C. Piefke, O. E. Peil, and F. Lechermann, Phys. Rev. B **86**, 155121 (2012).

[39] F. Lechermann, W. Körner, D. F. Urban, and C. Elsässer, Phys. Rev. B **100**, 115125 (2019).

[40] C. Elsässer, N. Takeuchi, K. M. Ho, C. T. Chan, P. Braun, and M. Fähnle, J. Phys.: Condens. Matter **2**, 4371 (1990).

[41] F. Lechermann, F. Welsch, C. Elsässer, C. Ederer, M. Fähnle, J. M. Sanchez, and B. Meyer, Phys. Rev. B **65**, 132104 (2002).

[42] B. Meyer, C. Elsässer, F. Lechermann, and M. Fähnle, *FOR-TRAN 90 Program for Mixed-Basis-Pseudopotential Calculations for Crystals*, Max-Planck-Institut für Metallforschung, Stuttgart (1998).

[43] W. Körner and C. Elsässer, Phys. Rev. B **81**, 085324 (2010).

[44] J. P. Perdew and A. Zunger, Phys. Rev. B **23**, 5048 (1981).

[45] W. M. Temmerman, Z. Szotek, and H. Winter, Phys. Rev. B **47**, 11533 (1993).

[46] V. I. Anisimov, J. Zaanen, and O. K. Andersen, Phys. Rev. B **44**, 943 (1991).

[47] J. Zaanen, G. A. Sawatzky, and J. W. Allen, Phys. Rev. Lett. **55**, 418 (1985).

[48] M. Imada, A. Fujimori, and Y. Tokura, Rev. Mod. Phys. **70**, 1039 (1998).

[49] M. J. Han, X. Wang, C. A. Marianetti, and A. J. Millis, Phys. Rev. Lett. **107**, 206804 (2011).

[50] B. Amadon, F. Lechermann, A. Georges, F. Jollet, T. O. Wehling, and A. I. Lichtenstein, Phys. Rev. B **77**, 205112 (2008).

[51] V. I. Anisimov, I. V. Solovyev, M. A. Korotin, M. T. Czyżyk, and G. A. Sawatzky, Phys. Rev. B **48**, 16929 (1993).

[52] P. Werner, A. Comanac, L. de'Medici, M. Troyer, and A. J. Millis, Phys. Rev. Lett. **97**, 076405 (2006).

[53] O. Parcollet, M. Ferrero, T. Ayral, H. Hafermann, I. Krivenko, L. Messio, and P. Seth, Comput. Phys. Commun. **196**, 398 (2015).

[54] P. Seth, I. Krivenko, M. Ferrero, and O. Parcollet, Comput. Phys. Commun. **200**, 274 (2016).

[55] J. E. Gubernatis, M. Jarrell, R. N. Silver, and D. S. Sivia, Phys. Rev. B **44**, 6011 (1991).

[56] H. J. Vidberg and J. W. Serene, J. Low. Temp. Phys. **29**, 179 (1977).

[57] J. Hirsch and F. Marsiglio, Physica C: Superconductivity and its Applications **566**, 1353534 (2019).

[58] B. Keimer, N. Belk, R. J. Birgeneau, A. Cassanho, C. Y. Chen, M. Greven, M. A. Kastner, A. Aharony, Y. Endoh, R. W. Erwin, and G. Shirane, Phys. Rev. B **46**, 14034 (1992).

[59] E. Dagotto, Rev. Mod. Phys. **66**, 763 (1994).

[60] M.-Y. Choi, K.-W. Lee, and W. E. Pickett, Phys. Rev. B **101**, 020503(R) (2020).

[61] H. Zhang, L. Jin, S. Wang, B. Xi, X. Shi, F. Ye, and J.-W. Mei, Phys. Rev. Research **2**, 013214 (2020).

[62] Y. Gu, S. Zhu, X. Wang, J. Hu, and H. Chen, Commun. Phys. **3**, 84 (2020).

[63] Z. Liu, Z. Ren, W. Zhu, Z. F. Wang, and J. Yang, npj Quantum Mater. **5**, 31 (2020).

[64] I. Leonov, S. L. Skornyakov, and S. Y. Savrasov, Phys. Rev. B **101**, 241108(R) (2020).

[65] X. Wan, V. Ivanov, G. Resta, I. Leonov, and S. Y. Savrasov, Phys. Rev. B **103**, 075123 (2021).

[66] R. Zhang, C. Lane, B. Singh, J. Nokelainen, B. Barbiellini, R. S. Markiewicz, A. Bansil, and J. Sun, arXiv:2009.05816.

[67] J. Kapeghian and A. S. Botana, Phys. Rev. B **102**, 205130 (2020).

[68] M. A. Hayward, M. A. Green, M. J. Rosseinsky, and J. Sloan, J. Am. Chem. Soc. **121**, 8843 (1999).

[69] G.-M. Zhang and L. Yu, Phys. Rev. B **62**, 76 (2000).

[70] L. Isaev and I. Vekhter, Phys. Rev. Lett. **110**, 026403 (2013).

[71] B. H. Bernhard and C. Lacroix, Phys. Rev. B **92**, 094401 (2015).

[72] H. Li, Y. Liu, G.-M. Zhang, and L. Yu, J. Phys.: Condens. Matter **27**, 425601 (2015).

[73] J. Karp, A. Hampel, M. Zingl, A. S. Botana, H. Park, M. R. Norman, and A. J. Millis, Phys. Rev. B **102**, 245130 (2020).

[74] J. Karp, A. Hampel, and A. J. Millis, arXiv:2102.08522.

[75] F. Bernardini and A. Cano, J. Phys. Mater. **3**, 03LT01 (2020).

[76] B. Geisler and R. Pentcheva, Phys. Rev. B **102**, 020502(R) (2020).

[77] R. He, P. Jiang, Y. Lu, Y. Song, M. Chen, M. Jin, L. Shui, and Z. Zhong, Phys. Rev. B **102**, 035118 (2020).

[78] Y. Zhang, L.-F. Lin, W. Hu, A. Moreo, S. Dong, and E. Dagotto, Phys. Rev. B **102**, 195117 (2020).

[79] A. S. Botana, F. Bernardini, and A. Cano, JETP **159**, 711 (2021).

[80] V. Olevano, F. Bernardini, X. Blase, and A. Cano, Phys. Rev. B **101**, 161102(R) (2020).